Hindawi
International Journal of Antennas and Propagation
Volume 2024, Article ID 3080895, 14 pages
https://doi.org/10.1155/2024/3080895

Research Article

Wireless Channel Model Based on Ray Tracing Algorithm in the Sea Environment

Zhongyu Liu, Qi Yao, Quanqing Li, Lixin Guo, and Shuo Hu

School of Physics, Xidian University, Xi'an, Shaanxi 710071, China

Correspondence should be addressed to Zhongyu Liu; liuzy@xidian.edu.cn

Received 27 July 2023; Revised 3 January 2024; Accepted 8 January 2024; Published 20 January 2024

Academic Editor: Arpan Desai

The maritime environment is complex and changeable, and an accurate maritime wireless channel model is particularly difficult to establish. This study investigates the sensitivity of a three-dimensional (3D) maritime ray tracing (RT) model for the use of the geometrical optics in radio channel characterizations of maritime environments. The channel measurement experiments are mainly carried out at three frequency points of 1.5, 1.8, and 2.5 GHz, and the simulation results of the model are compared and corrected with the measured received power. Analysis shows that the modified model simulation results at 1.5, 1.8, and 2.5 GHz frequency points are in good agreement with the actual measurement, and the RMS is within 7 dB. Moreover, the reverse RT algorithm has the advantages of fast calculation speed and high efficiency. The effects of the different sea conditions, frequencies, and distances on the propagation of electromagnetic waves are analyzed on the basis of this model.

1. Introduction

With the increase in maritime activities, maritime wireless communication has attracted the attention of researchers from all over the world. In the past few decades, wireless channel models in urban areas and indoor environments have been improved. However, electromagnetic wave propagation is easily affected by ocean waves and atmospheric ducts due to the complex and changeable maritime environment. Thus, an accurate maritime wireless channel model must be established.

1.1. Related Works. The currently widely used wireless channel models include the Longley–Rice model, ITU-R P.1546 model, two-ray model, and three-ray model. The two-ray model believes that only the direct path and specular reflection of electromagnetic waves need to be considered in the sea environment. The three-ray model includes the direct path, specular reflection path, and secondary reflection path or scattering path of electromagnetic waves. Different correction methods are also proposed for the various application scenarios.

Mo et al. [1, 2] tested and verified that the Longley–Rice model is biased when it is directly applied to the sea surface channel prediction. Zhang et al.[3] tested the shore-sea environment, and the carrier frequency was 2 GHz. The aforementioned reference compared the RSL obtained by the test with the Okumura–Hata model, the COST 231 Hata model, and the ITU-R P.1546-2 model. The study found that the ITU-R P.1546-2 model of the open cold sea exceeding the field strength values best matches the measurements at 50% position. Zaidi et al. [4] tested the 2.58 GHz frequency point and compared it with the ITU-R P.1546-3 model, which proved that the model has a high degree of matching with the measured results. Xi et al. [5] used the 28 GHz frequency point in the CW wave to the shore-ship environment to conduct measurement experiments. The literature found that the simulation results of the ITU-R P.1546 model did not match the measured data, and the prediction results of the two-path model were consistent with the overall measured data.

Reyes-Guerrero [6] placed the transmitting antenna on the buoy and the receiving antenna on the boat and tested it at the seaside near the urban area. The results showed that the double-path model can be used for prediction in the case

of line of sight and has a significant influence, and the effect of the antenna pattern needs to be considered in the model prediction. Wang et al. [7, 8] placed the transmit antenna on the ship and the receive antenna on the shore and tested the frequency with a 5.2 GHz bandwidth of 100 MHz. In a port environment, the radio link between the ship and the shore depends on the geometry of the environment. A two-path model can be used to simulate the path loss over line-of-sight sea surfaces. Mehrnia and Ozdemir [9] found that the two-path model and the free-space model are suitable for predicting electromagnetic wave transmission under low-frequency signals. The two-path model is still very reliable under high-frequency signals, such as 35 and 94 GHz, when the distance between the transceivers is less than 2 km. However, the two-path model cannot be used for predictive analysis after the distance exceeds 2 km. Accordingly, the literature revised the two-path model and introduced an exponential parameter to predict the last peak of the path loss. The revised two-path model can be used in adaptive high-frequency channel prediction.

Researchers conducted measurement experiments on 1.9 GHz maritime broadband wireless channels near the Aegean Sea in Greece [10]. The measurement results demonstrated that the large-scale path loss is related to the propagation environment and antenna height. Meanwhile, the small-scale multipath delay distribution is related to the properties of the scatter. The delay parameter significantly increases in the NLOS case, which cannot be directly modeled with simple mathematical expressions. Jo et al. [11] measured the received signal power on the Korean coastline and compared the measured RSRP value with the three traditional path loss models: free space path loss, two-ray path loss, and Okumura–Hata. The comparison results showed that the models tend to underestimate the impact of the marine environment on RSRP, and significant differences can be observed between experimental data and path loss models. Li et al. [12] conducted wireless channel measurement and analysis on the shipping environment and found that bridges, buildings, and large ships would have a significant influence on wireless channels. They conducted channel measurements on wireless channels between ship-to-ship and ship-to-infrastructure [13, 14]. The results showed that the main factor affecting the root mean square delay spread in the maritime wireless channel without other obstacles is the communication between transmitting and receiving. In terms of the propagation path loss, the sea surface reflection, scattering, water surface shadow, atmospheric refraction, and atmospheric ducts are the key influencing factors. Furthermore, the diffraction loss caused by the curvature of the earth cannot be ignored for the long-distance wireless communication at sea.

According to the abovementioned literature, the Longley–Rice model cannot be directly applied in the marine environment. The ITU-R P.1546 model is in good agreement in certain scenarios. Meanwhile, the two-path model is more suitable for predicting electromagnetic waves in the case of sight distance and low frequency, but it needs to be corrected in certain cases. The two-path model can be used when the sea surface is calm. Meanwhile, the three-path model is more applicable when the sea surface greatly fluctuates. The radio channel prediction model in marine environment based on ray tracing algorithm is usually a forward method [15], and the reverse method is rarely studied.

1.2. Challenges and Proposed Methods. Obviously, the current radio wave propagation model in the marine environment faces the following problems. (i) The radio wave propagation problem in the marine environment with different wind speeds and different frequencies cannot be accurately solved by the existing models. (ii) Under the efficiency of the general electromagnetic calculation method in the large-scale marine environment, there is still a problem that the error of the radio wave propagation path increases with the increase of distance, which further leads to the large error of the calculation results of the time delay and phase. (iii) Most models cannot be extended to the radio wave propagation model in the marine-near-Earth environment, the marine-multitarget environment, and other conditions, and their scalability and practicability are poor.

To solve these problems, the innovative points of this paper are as follows. (i) A radio wave propagation model in marine environment with different wind speeds and different frequencies is established. (ii) It solves the problem that the radio wave propagation path error increases with the increase of distance in the general electromagnetic computing model in large-scale marine environment, and the calculation of time delay and phase is more accurate. (iii) Compared with most models that cannot be extended to ocean-near-Earth environment and ocean-multitarget environment, this model is more scalable and practical.

This work proposes a maritime wireless channel model based on a reverse RT algorithm, which is a deterministic model. The other chapters of this paper are arranged as follows: in the second section, the sea surface environment is first modeled, then all paths of sea electromagnetic wave propagation are obtained according to the RT algorithm, and finally the path loss, received power, and small-scale fading information are calculated according to the effective ray path. The third section compares the model results with the measured results. The fourth section presents the simulation analysis of the model, and the fifth section provides the summary.

2. Propagation Model

2.1. Dynamic Sea Modeling. A dynamic sea surface environment model must be established because the sea surface shape is complex and changeable, and the wave height dynamically changes with the force factors on the sea surface. The existing wave spectra are all empirical models based on a large number of ocean observation data. The Pierson–Moskowitz (PM) sea spectrum is a steady-state wave spectrum, has a good data base, and is convenient for analysis and processing.

Accordingly, the PM sea spectrum is used for sea surface modeling in this work [16]. A 2D random sea surface is generated on the basis of the Monte Carlo method [17].

Every triangular surface element contains three vertex coordinates, normal vector (for occlusion judgment), center coordinates, and other information, as shown in Figure 1.

In this work, the sea surface electrical parameters are described by the Debye formula. The relative permittivity of seawater is related to seawater temperature, carrier frequency, and seawater salinity. Refer to literature [18, 19] for further details. The relative permittivity of seawater decreases with the increase in frequency and salinity. When the seawater temperature is 0°C–5°C, it first increases and then decreases. When the seawater temperature is greater than 5°C, the relative permittivity increases with the increase in seawater temperature. The conductivity of seawater is related to seawater temperature and salinity. Specifically, the conductivity of seawater increases with the increase in seawater salinity and decreases with the increase in seawater temperature. Therefore, the actual sea water salinity, temperature, and carrier frequency should be considered when modeling the sea surface.

2.2. Sea Surface Reflection Coefficient. The reflection of radio waves on calm seas is mainly specular reflection. The Fresnel reflection coefficients of the horizontally and vertically polarized waves on smooth seas are shown in (1) and (2) according to Snell's law [20]:

$$R_H = \frac{\sin\theta - \sqrt{\tilde{\varepsilon} - \cos^2\theta}}{\sin\theta + \sqrt{\tilde{\varepsilon} - \cos^2\theta}}, \tag{1}$$

$$R_V = \frac{\tilde{\varepsilon}\sin\theta - \sqrt{\tilde{\varepsilon} - \cos^2\theta}}{\tilde{\varepsilon}\sin\theta + \sqrt{\tilde{\varepsilon} - \cos^2\theta}}, \tag{2}$$

where θ is the grazing incidence angle and $\tilde{\varepsilon}$ is the relative permittivity of seawater.

When the sea state level is high, the sea surface is no longer calm, and radio waves will generate scattering paths when propagating on the rough sea surface. The reflection coefficient on the rough sea surface needs to be multiplied by the roughness correction coefficient before the reflection coefficient on the smooth sea surface [21], as shown in the following equation:

$$\rho = \frac{1}{\sqrt{3.2g - 2 + \sqrt{(3.2g)^2 - 7g + 9}}}, \tag{3}$$

$$g = 0.5\left(\frac{4\pi\sigma_h f \sin\theta}{c}\right)^2, \tag{4}$$

where c is the speed of light, λ is the wavelength of the radio wave, and σ_h is the rms height of the sea surface, which can be given according to the Phillips wave model:

$$\sigma_h = 0.0051w^2, \tag{5}$$

where w is the wind speed near the sea surface.

2.3. Multipath Determination Based on RT. This work uses the reverse RT algorithm to judge whether direct and reflected paths exist. The influence of direct and reflected rays in the marine line-of-sight environment is the key component. The ray paths calculated in this work are divided into direct paths, primary reflection paths, and secondary reflection paths. These types of ray paths are determined through the following steps:

(1) The visible relationship between all grids is prejudged in combination with the normal vector direction of the triangular surface element of the environment model according to the position of the transmitting antennas (TX) and receiving antennas (RX). These surface elements that satisfy the visible relationship are stored to accelerate RT. The model determines the computational efficiency of multiple reflections from the sea surface.

First, the calculation range is determined according to the position of TX and RX, as shown in Figure 2. The triangle in Figure 2 represents the TX and RX, and the rectangular area is the calculation area. In the subsequent steps, only the grid in the rectangular area is determined. The other parts are no longer calculated regardless of whether the grid intersects the ray.

Then, a shadow test is performed on the grid and radiation source, as shown in Figure 3. The angle relationship between the ray direction and the normal vector of the triangular surface element is determined, wherein $\overrightarrow{S}$ is the ray direction and $\overrightarrow{n}$ is the normal vector of the triangular surface element. When $\overrightarrow{S} \cdot \overrightarrow{n} < 0$, the ray and the triangular facet are in the same plane, the triangular facet is considered to be visible, and the facet is stored; otherwise, the triangular facet is discarded.

Finally, the intersection of the ray and the surfel is determined. Suppose the rays are

$$\overrightarrow{X} = \overrightarrow{S_i}t + \overrightarrow{T}\ (t \geq 0), \tag{6}$$

where $\overrightarrow{T}$ is the starting point of the ray; $\overrightarrow{S_i}$ is the ray direction; and P_1, P_2, and P_3 are the three vertices of the triangular surface element, as shown in Figure 4. The direction vector $\overrightarrow{S_i}$ can be expressed as

$$\overrightarrow{S_i} = l\overrightarrow{\mathrm{TP}_1} + m\overrightarrow{\mathrm{TP}_2} + n\overrightarrow{\mathrm{TP}_3}, \tag{7}$$

where l, m, and n are the coordinates of the vector in the space oblique coordinate system with $\overrightarrow{\mathrm{TP}_1}$, $\overrightarrow{\mathrm{TP}_2}$, and $\overrightarrow{\mathrm{TP}_3}$ as the base vectors, respectively. When l, m, and n are all greater than zero, they are judged as intersecting.

This study determines the intersection of the ray and the plane where the triangle is located, which is the intersection of the ray and the triangle.

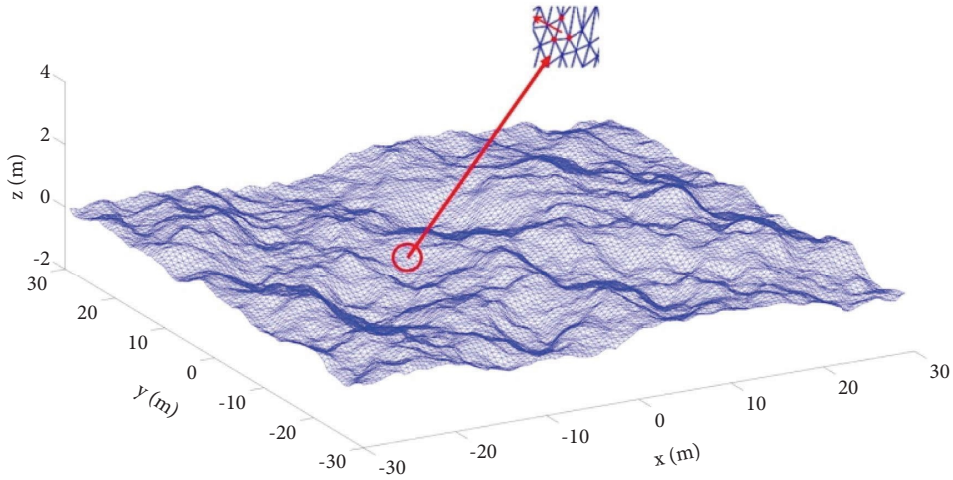

Figure 1: Sea surface when the wind speed is 8 m/s and the wind direction is 0°.

The surfels obtained through the abovementioned three steps are the visible surfels and are stored.

(2) This study determines whether the direct path, the primary reflection path, and the secondary reflection path exist. The corresponding flowchart is shown in Figure 5.

Determine whether there is a direct path.

Determine whether there is a surfel occlusion between TX and RX; if not, then the direct path exists; if there is, then it does not exist.

The calculation steps of the primary reflection path are as follows:

(1) Calculate the visible surface elements of TX and RX according to step (1), denoted as TX_visible and RX_visible.

(2) Calculate the mirror point of TX for each panel in TX_visible and set it as TX_MIR.

(3) Calculate the unit direction vector of the connection between TX_MIR and RX, and judge whether the connection has an intersection with the surface element in RX_visible.

(4) If an intersection exists, then calculate the coordinates of the intersection on the surface element and record it as a reflection point; if no intersection exists, then no primary reflection can be found.

The calculation steps of the secondary reflection path are as follows:

(1) Calculate the mirror point of the transmit point of the surface element in TX_visible and set it as TX_MIR.

(2) Calculate the mirror point of TX_MIR of the surface element in RX_visible and set it as RX_MIR.

(3) Calculate whether the ray connecting RX_MIR and RX has an intersection with the surface element in RX_visible. If an intersection point exists, then find the coordinates of the intersection point on the surface element and record it as SECOND_REF; if it does not exist, then no secondary reflection path can be found.

(4) Determine whether an intersection exists between the ray connecting SECOND_REF and TX_MIR and the surface element in TX_visible. If an intersection exists, then find the coordinates of the intersection and record it as FIRST_REF; if a secondary reflection path exists and its reflection points are FIRST_REF and SECOND_REF, then no secondary reflection path can be found.

All the obtained paths are stored in the virtual source tree [22] and combined with the antenna patterns of the transmitting and receiving antennas. The relevant electromagnetic calculations are performed through these paths, and the final field of each path can be obtained. The total field and received power can be obtained by superimposing the vectors. It is worth mentioning that in the current study, the Tx and Rx are situated in regions close to the sea surface, and preliminary experiments encountered certain challenges, resulting in a smaller quantity of gathered data samples. Consequently, this study has not considered the impacts of atmospheric refraction and atmospheric ducting, implying that the calculations for refraction are based on the principle of free space.

3. Measurement Campaign

3.1. Test Environment. This work was tested at the seaside of Lianyungang, China, from November 1st to 3rd, 2020. The environment and equipment of the transmitting and receiving points are shown in Figure 6. The device connection diagram is shown in Figure 7.

The transmitting and receiving antennas use the same type of horn antenna, and the graph of their gain versus frequency is shown in Figure 8.

The antenna pattern of the measured horn antenna is extracted and simulated to better match the simulation results with the measured results. The antenna patterns of

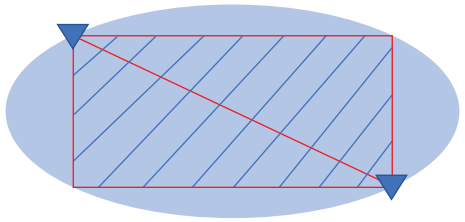

Figure 2: Schematic diagram of narrowing the judgment range of RT calculation.

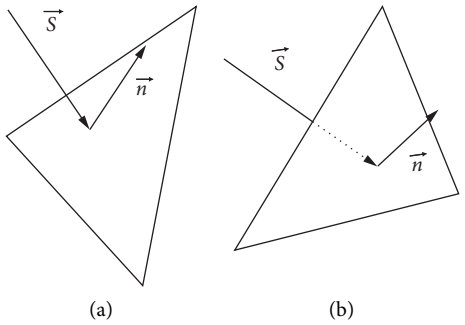

Figure 3: Shadow test schematic. (a) Visible. (b) Invisible.

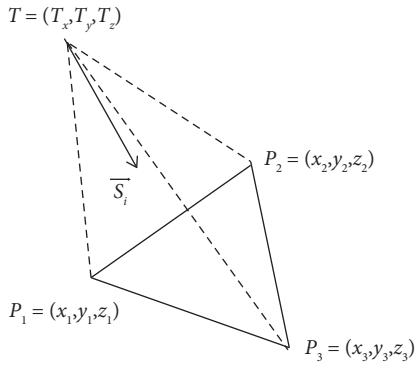

Figure 4: Schematic of the triangle intersection algorithm.

the horn antenna in each frequency band from 1 GHz to 8 GHz are inconsistent. In this work, 1.5, 1.8, and 2.5 GHz are tested. The antenna patterns up to 1.5 and 2.5 GHz are used herein, as shown in Figure 9.

According to antenna at the 1.5 and 2.5 GHz frequency points, the 3D radiation pattern of the horn antenna is calculated on the basis of the method in [23].

This work performs tests on the long bridge at intervals, as shown in Figure 10. The position coordinates and antenna height of each receiving test point are recorded. The sea surface wind speed, salinity, temperature, and sea surface height changes during each test are also recorded. Moreover, the position coordinates and height information of the transmitting antenna are recorded. The distance between the receiving and transmitting antennas of each test point is shown in Figure 11, and the height of the receiving antenna of each test point is presented in Figure 12.

3.2. Comparison between the Simulation Results and the Actual Measurement. In order to study the radio wave propagation characteristics in the Sub-6 GHz band and verify the proposed model, this paper carried out a practical measurement activity. The test frequencies are 1.5, 1.8, and 2.5 GHz, in view of the less interference in the Sub-6 GHz band. The specific data are shown in Table 1.

The received power is computed for the following three distinct scenarios: direct line of sight (LOS), LOS with a single reflection (1-Ray), and LOS with up to two reflections (2-Ray). These calculated values are then juxtaposed with the experimental data, as depicted in fig. 13, while RMS values are tabulated in Table 2 for reference.

Figure 13 shows that under the 1.5 GHz frequency, the simulated data are about 5–10 dB smaller than the measured data when the distance between the transmitting and receiving antennas is greater than 4 km. When the distance is

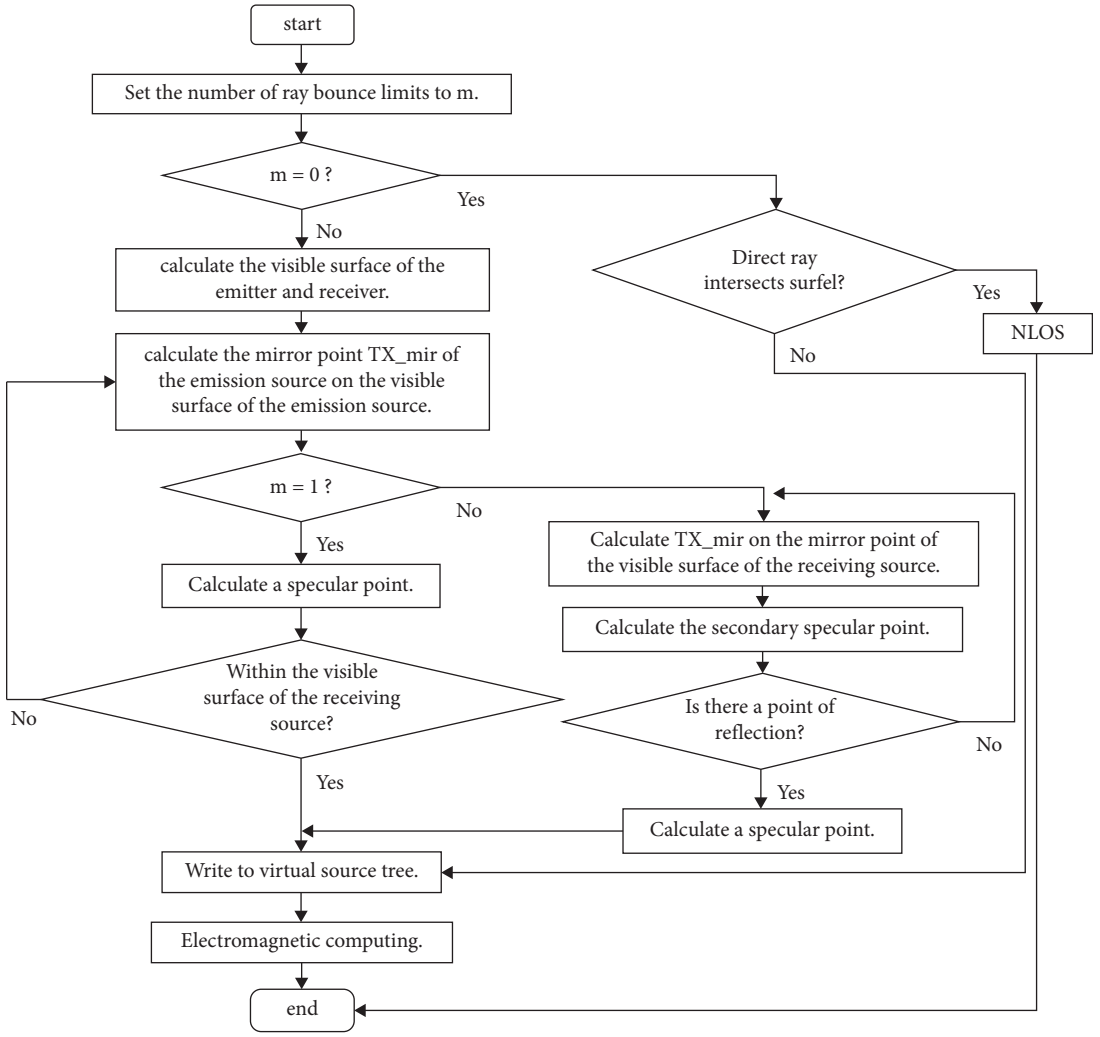

Figure 5: RT algorithm flowchart.

(a) (b)

Figure 6: Antenna. (a) TX. (b) RX.

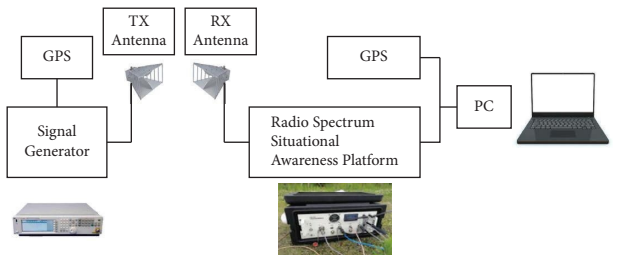

Figure 7: Device connection diagram.

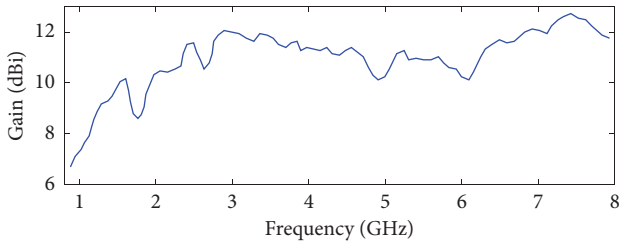

Figure 8: Antenna gain versus frequency plot.

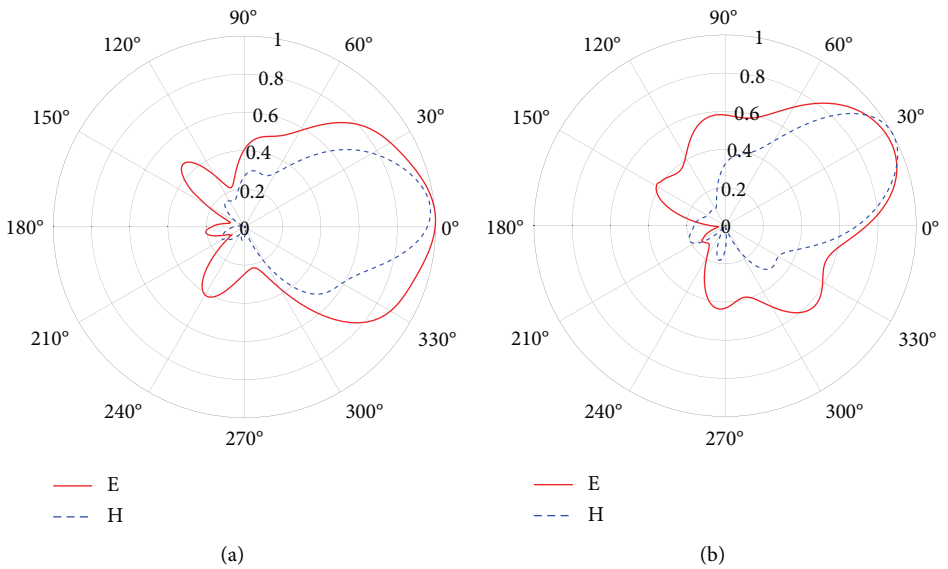

Figure 9: Antenna pattern when the carrier frequencies are (a) 1.5 GHz and (b) 2.5 GHz.

Figure 10: Measured test point placement diagram.

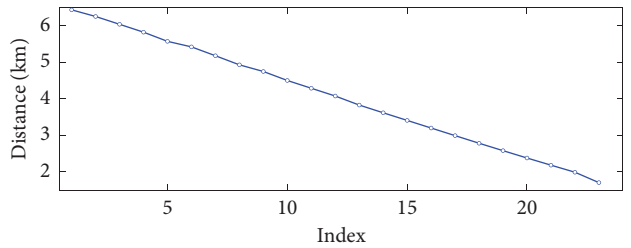

Figure 11: Schematic of the distance between the transmitting antenna and the receiving antenna.

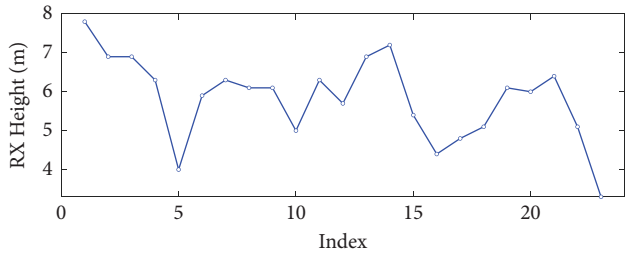

Figure 12: Receiving antenna height variation diagram.

Table 1: Parameter values.

Parameters	Values
Frequency (GHz)	1.5\1.8\2.5
Transmit power	30 dBm
TX antenna height	7.05 m
RX antenna height	As shown in Figure 12
Distance between TX and RX	As shown in Figure 11
Types of TX and RX	Horn antenna (the antenna pattern is shown in Figure 9)
Wind speed	2 m/s
Wind direction	30°
Sea temperature	20.15 (°C)
Seawater salinity	21.8 (ppt)
Number of subdivisions of sea surface elements	256 ∗ 256
RX antenna height	As shown in Figure 12
Distance between TX and RX	As shown in Figure 11
Types of TX and RX	Horn antenna (the antenna pattern is shown in Figure 9)
Wind speed	2 m/s

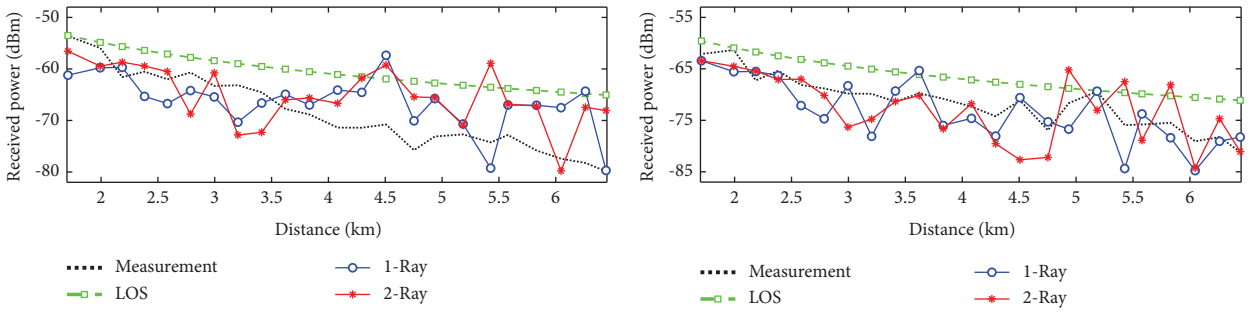

Figure 13: Continued.

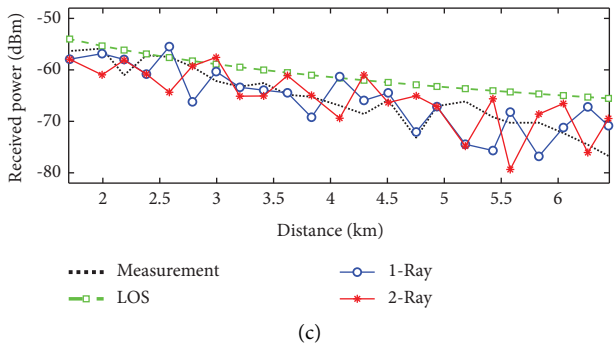

(c)

Figure 13: Comparison of the measured and simulated received power when the frequencies are (a) 1.5 GHz, (b) 1.8 GHz, and (c) 2.5 GHz.

Table 2: Simulated and measured received power RMS.

Frequency (GHz)	LOS	LOS + one-ray RMS (dB)	LOS + two-ray RMS (dB)
1.5	8.9415	6.6057	7.4984
1.8	5.5256	4.0090	4.8498
2.5	5.3818	4.1058	4.8157

less than 4 km, the simulation curves of the two reflections are closer to the actual data. When the frequency is 1.8 GHz, the simulation data jump at every interval. Overall, the data of one reflection are in better agreement. When the frequency is 2.5 GHz, the simulation data as a whole fluctuate near the measured data. When the distance is greater than 5 km, the simulation data of the two reflections greatly fluctuate.

Table 2 illustrates that the RMS of the two reflections is small when the frequencies are 1.5 and 1.8 GHz. Meanwhile, the RMS of the first reflection is small when the frequency is 2.5 GHz.

Given that measurement errors may occur in the test, eight points are selected around the test point for simulation operation. These eight points are averaged with the power simulation value of the test point, which is regarded as the smoothing process (Figure 14). The comparison between the smoothed data results and the measured data is shown in Figure 15, and the RMS is illustrated in Table 3.

Figure 15 illustrates that the simulation data floating tends to be flat after the smoothing process. When the distance between the transmitting and receiving antennas is less than 3.5 km, the simulation data are smaller than the measured data as a whole when the frequency is 1.5 GHz.

When the distance is greater than 3.5 km, the simulation curves of the two reflections are in good agreement with the measured data. When the distance is less than 4.2 km, the simulated data are basically consistent with the measured data when the frequency is 1.8 GHz. The simulated data of one reflection are in better agreement with the measured data when the distance increases. When the frequency is 2.5 GHz, the simulation data are consistent with the measured data as a whole. When the distance is greater than 6 km, the difference between the data of one reflection and the measured data is slightly larger. Thus, the simulation curves of the two reflections are more consistent.

The comparison of Tables 2 and 3 indicated that only the RMS of one reflection at 1.5 GHz and the RMS of two reflections at 2.5 GHz decreased, and the others increased after smoothing. This phenomenon may be because the average value of the nearby power values is processed when the smoothing process is performed. Accordingly, the points with a large difference between the simulated received power and the measured value are smoothed out. Although the error of the individual points can be reduced, the accuracy is diminished.

In summary, the calculation results of the two reflections on the sea surface are more accurate, and the RMS is within 8 dB, which is in line with the industry standard.

4. Numerical Analysis

According to the revised model, the received power, impulse response, etc. are simulated and analyzed under different sea conditions, carrier frequencies, and distances between the transmitting and the receiving antennas.

4.1. Delay Resolution. In terms of the impulse response, the delay power of all paths cannot be displayed in the actual measurement due to the delay resolution of the instrument. In terms of the impulse response, the delay power of all paths cannot be displayed in the actual measurement due to the delay resolution of the instrument. In this work, at varying temporal sampling resolutions, the received power during the sampling time results from the superposition of multiple received electric fields within the corresponding time interval.

When the carrier frequency is 1.5 GHz, the transmit power is 1 W. The transmitting and receiving antennas are all half-wave dipole antennas. The heights of the transmitting and receiving antennas are 12 and 10 m, respectively. The distance between the transmitting and the receiving

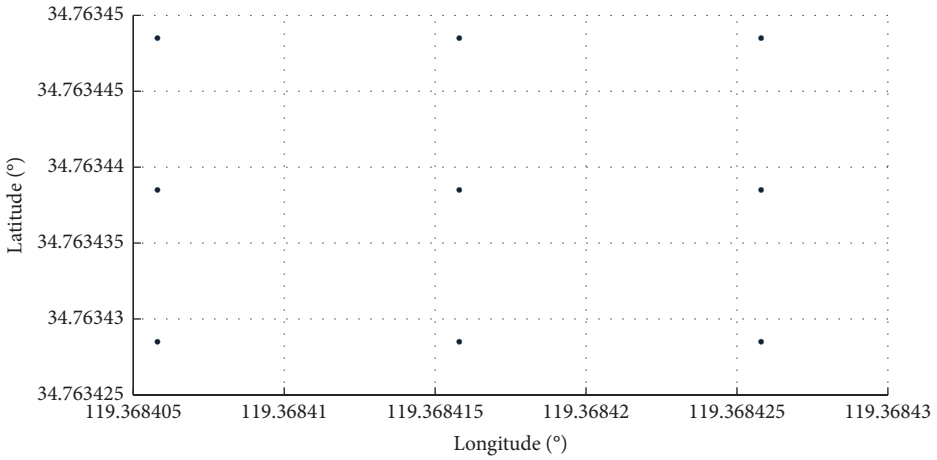

Figure 14: Schematic of smoothing processing of the measured points.

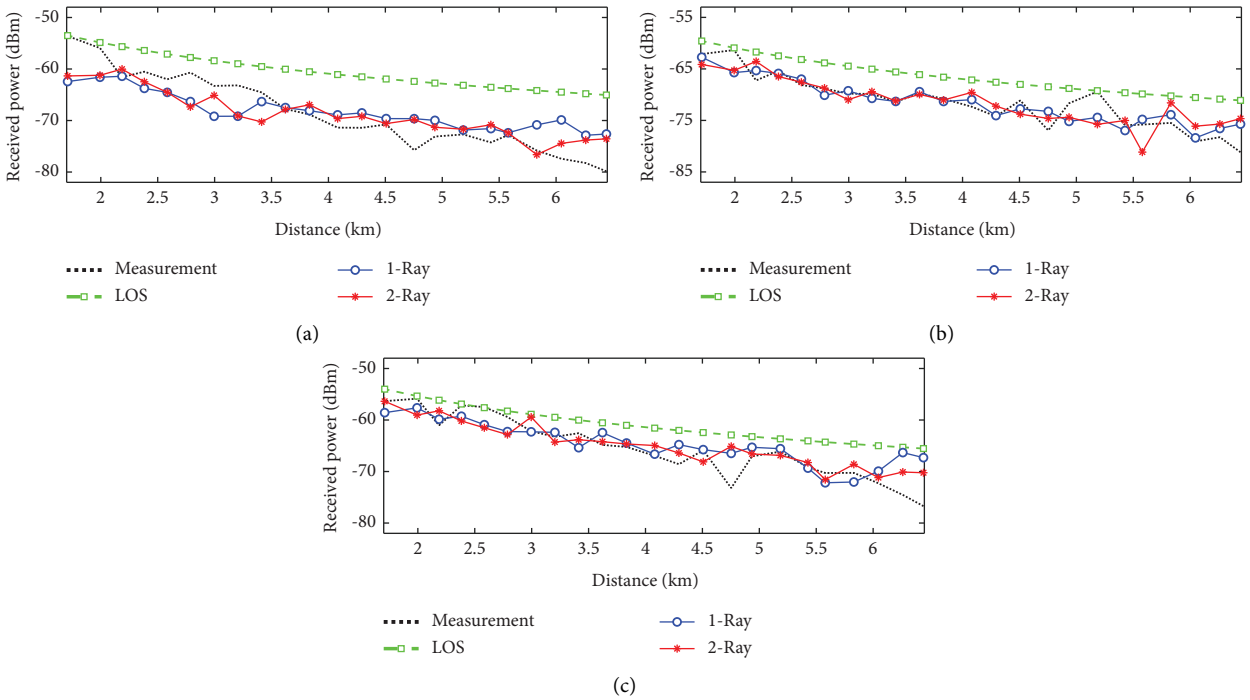

Figure 15: Comparison of measured received power and simulation after smoothing: (a) 1.5 GHz; (b) 1.8 GHz; (c) 2.5 GHz.

Table 3: RMS table of the measured received power and simulated received power after smoothing.

Frequency (GHz)	LOS	LOS + one-ray RMS (dB)	LOS + two-ray RMS (dB)
1.5	8.9415	4.5081	3.8931
1.8	5.5256	2.2966	3.0239
2.5	5.3818	3.4912	3.0519

antennas is 5 km, the seawater temperature is 20°C, the seawater salt is 34.7%, the wind speed at 10 m offshore is 5 m/s, and the offshore wind direction is 0°. The impulse response graphs at different resolutions are shown in Figure 16.

Figure 16 shows that the larger the resolution, the sparser the displayed impulse response. However, the main diameters are preserved, and some diameters with lower power are filtered out. Accordingly, the impulse response can be adjusted by changing the resolution. The resolution corresponding to the actual measurement equipment is selected when comparing with the measured multipath data.

4.2. Wind Speed and Direction. The sea surface wind direction takes the x-axis as the wind direction of 0°, which is the downwind, and the wind direction angle θ is the angle between the x-axis and the y-axis. The schematic is shown in Figure 17.

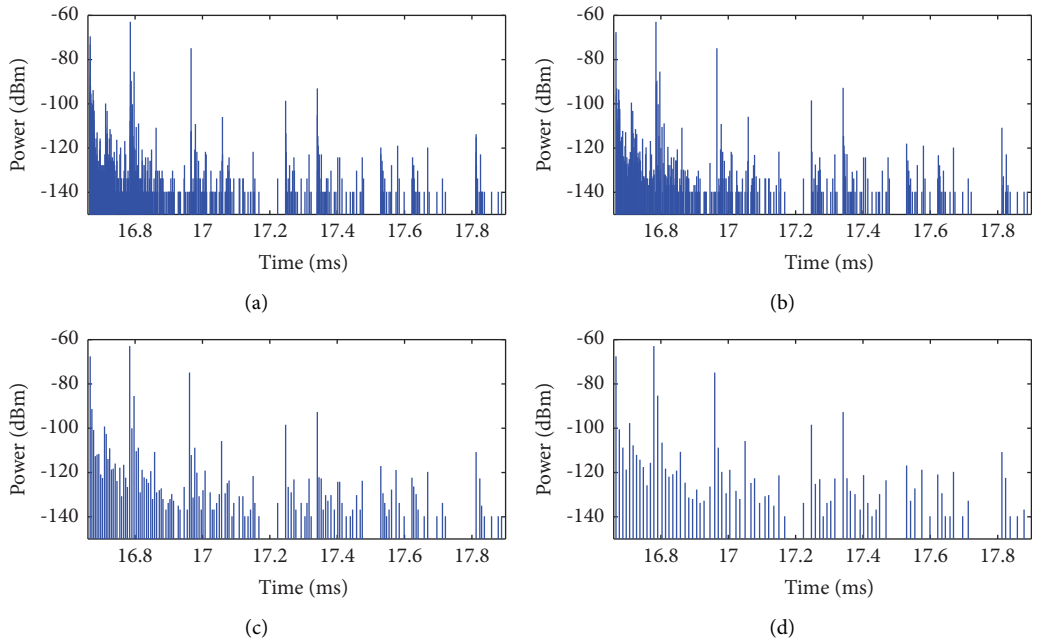

Figure 16: Impulse response plots processed at different resolutions: (a) no resolution processing; (b) 1 ns; (c) 5 ns; (d) 10 ns.

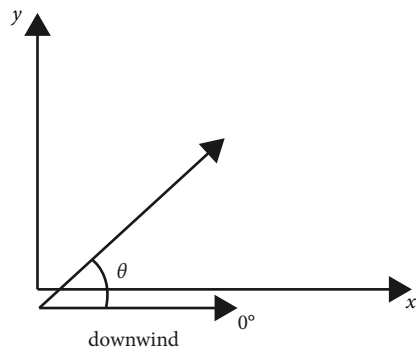

Figure 17: Wind direction diagram.

The carrier frequency is 2.5 GHz, and the transmit power is 1 W. The transmitting and receiving antennas are all half-wave dipole antennas. The heights of the transmitting and receiving antennas are 12 and 10 m, respectively. The distances between the transmitting and receiving antennas are 1, 5, and 10 km, the seawater temperature is 20°C, the seawater salinity is 34.7%, and the offshore wind directions are 0°, 30°, 90°, and 180°, respectively. The wind speed at a height of 10 m at sea gradually increases from 0 m/s to 14 m/s, as shown in Figure 18.

Figure 18 demonstrates that the received power does not change when the wind speed is less than 1 m/s. Meanwhile, the received power fluctuates with the increase in wind speed. When the wind direction increases, the received power drastically changes. When the wind is blowing in the opposite direction, the received power more dramatically changes than when the wind is down, and the received power loss is about 10 dB. When the wind direction is downwind, the received power fluctuates within 10 dB. When the wind direction is headwind, the received power generally decreases with the increase in the wind speed. This phenomenon may be because the sea level increases with the increase in the wind speed, which affects the propagation of electromagnetic waves.

When the wind speed is greater than 1 m/s, the received power will be affected regardless of the distance between the transceiver antennas. When the wind speed is greater than 6 m/s, the received power more drastically changes. The resulting loss is greater with the increase in the distance between the transceiver antennas. The received power amplitude more greatly changes with the increase in the wind direction angle. The larger the distance between the transceiver antennas, the larger the wind direction angle, and the overall received power shows a downward trend.

4.3. Frequency. When the transmit power is 1 W, the transmitting and receiving antennas are all half-wave dipole antennas. The heights of the transmitting and receiving antennas are 12 and 10 m, respectively. The seawater

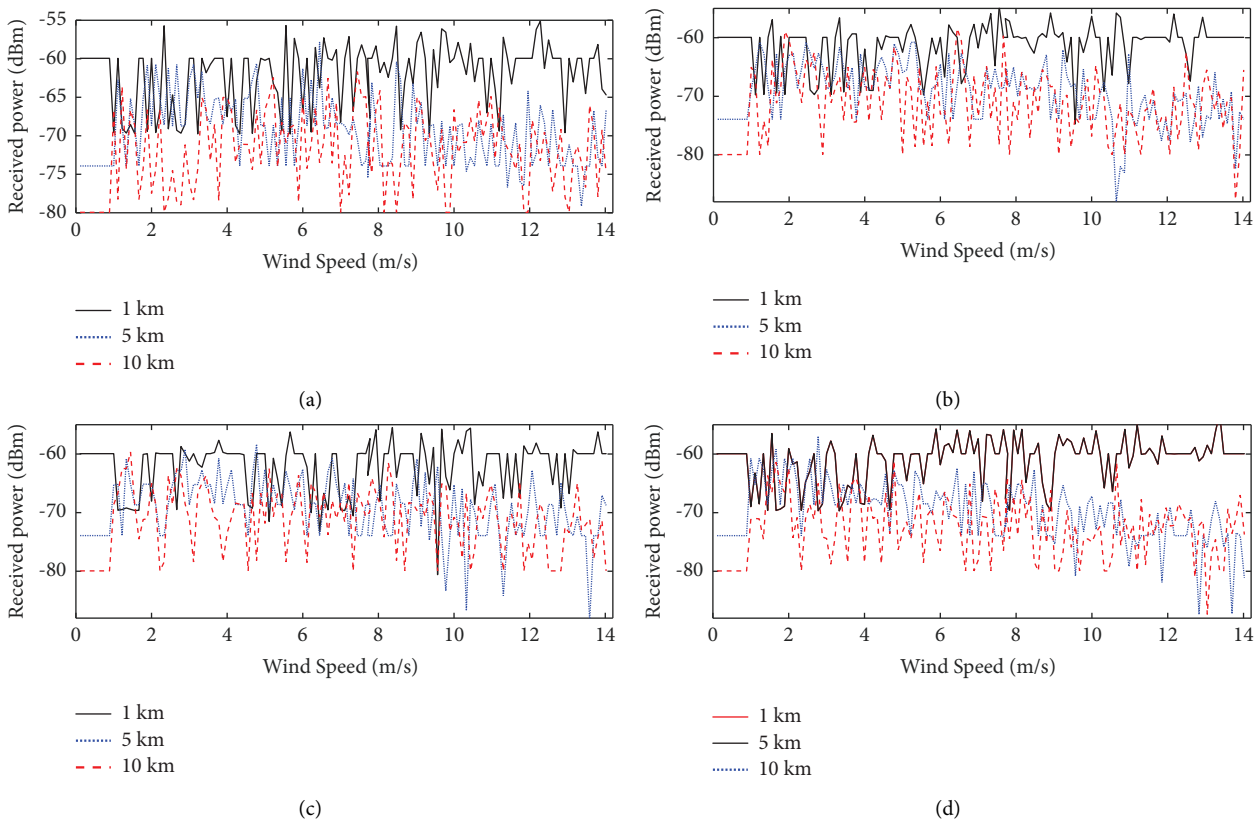

Figure 18: Variation of received power with frequency in different wind directions and different wind speeds: (a) 0°; (b) 30°; (c) 90°; (d) 180°.

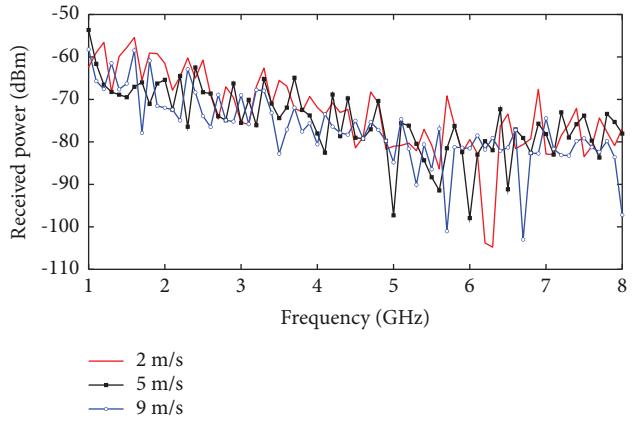

Figure 19: Variation of received power with frequency under different wind speeds.

temperature is 20°C, the seawater salinity is 34.7%, and the offshore wind direction is 0°. The 2–4 sea conditions are selected for simulation analysis according to the classification of sea conditions. The wind speed when the sea condition is grade 2 is set as 2 m/s. Meanwhile, the wind speed when the sea condition is at grade 3 is set as 5 m/s. When the wind speed is 9 m/s and the wind level is 4, the received power varies with the carrier frequency, as shown in Figure 19.

Figure 19 shows that the received power shows a downward trend as a whole with the increase in the carrier frequency. When the sea surface wind speed is 2 m/s, the received power is about 1 dB higher than the received power under other wind speed conditions. The higher the wind speed, the smaller the received power, but the effect is not obvious; when the frequency is greater than 5 GHz, the change of the received power amplitude becomes larger, and the fluctuation is more severe.

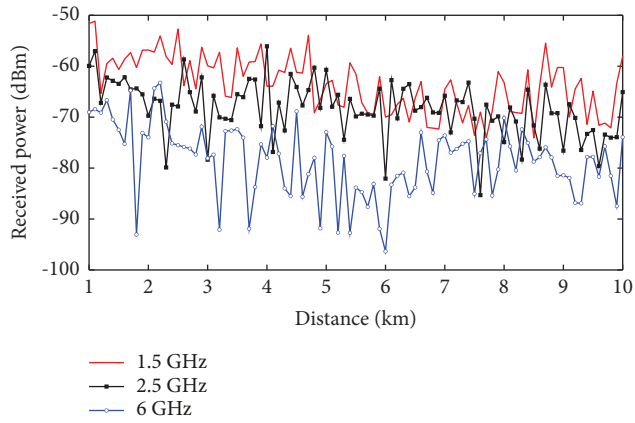

Figure 20: When the frequency is 1.5 GHz, 2.5 GHz, and 6 GHz, the received power varies with distance.

4.4. Distance. When the carrier frequencies are 1.5, 2.5, and 6 GHz, the transmit power is 1 W, and the transceiver antennas are all half-wave dipole antennas. The heights of the transmitting and receiving antennas are 12 and 10 m, respectively. The seawater temperature is 20°C, and the seawater salinity is 34.7%. The wind speed at a height of 10 m at sea is 5 m/s, the wind direction is 0°, and the distance between the transceiver antennas increases from 1 km to 10 km. The variation of received power with distance under different carrier frequencies is analyzed, as shown in Figure 20.

Figure 20 shows that the overall received power shows a downward trend with the increase in the distance between the transmitting and receiving antennas, while the received power decreases with the increase in frequency, which is in line with the actual situation. When the frequency is 6 GHz and the distance between the transceiver antennas is greater than 6 km, the received power increases. This phenomenon may be because the sea surface subdivision interval is fixed error in the ray path.

5. Conclusions

In this work, a maritime wireless channel model based on the RT algorithm is proposed, and the method of establishing the model is introduced. The channel measurement experiments are carried out at three frequency points of 1.5, 1.8, and 2.5 GHz in Lianyungang, China, and the model simulation and measured reception are analyzed and compared. The root mean square value of the calculated results and the measured results of the model with a maximum of two reflections is within 4 dB. This work also uses the model to simulate and analyze the influence of sea conditions, carrier frequency, and distance on the received power. The received power decreases with the increase in the offshore wind speed. When the wind direction changes from downwind to headwind, the received power decreases.

Herein, the measured offshore wind speed is low, the sea level is low, and only the received power is measured and analyzed. Further actual measurement comparison and verification of the sea environment under different sea conditions and multipath tests on the impulse response are necessary to improve the model.

Data Availability

The data used to support the findings of this study are available from the first author upon request.

Conflicts of Interest

The authors declare that they have no conflicts of interest.

Acknowledgments

This work was supported in part by the Key Project of Social Governance and Scientific and Technological Support for Smart Society (Grant No. 2022YFC3301403), Key Basic Research Project of the Foundation Strengthening Program, and Research Fund of Ministry of Education of China-China Mobile (Contract No. MCM20200302).

References

[1] H. Mo, B. Chen, and C. Shen, "Radio propagation prediction model for maritime mobile communication," in *Proceedings of the IET International Conference on Wireless Communications and Applications (ICWCA 2012)*, pp. 1–5, Kuala Lumpur, Malaysia, October, 2012.

[2] D. Liu, J. Nie, Y. Peng, and H. Xu, "A novel model for sea surface loss transport in complex environments," in *Proceedings of the 2023 International Applied Computational Electromagnetics Society Symposium (ACES-China)*, pp. 1–3, Hangzhou, China, August, 2023.

[3] J. Zhang, C. Li, J. Yang, and W. Chen, "Wireless propagation scene partitioning for inland waterway," in *Proceedings of the 2020 IEEE International Conference on Advances in Electrical Engineering and Computer Applications (AEECA)*, pp. 1040–1044, Dalian, China, August, 2020.

[4] K. S. Zaidi, V. Jeoti, A. Awang, and M. Drieberg, "High reliability using virtual MIMO based mesh network for maritime wireless communication," in *Proceedings of the 2016 6th International Conference on Intelligent and Advanced Systems (ICIAS)*, pp. 1–5, Kuala Lumpur, Malaysia, August, 2016.

[5] X. Liao, X. Li, Y. Wang, J. Zhou, T. Zhao, and J. Zhang, "Path loss modeling in urban water–land environments at 28 GHz: considering water surface reflection and building diffraction," *IEEE Antennas and Wireless Propagation Letters*, vol. 22, no. 4, pp. 744–748, 2023.

[6] J. C. Reyes-Guerrero, "Experimental broadband channel characterization in a sea port environment at 5.8 GHz," *IEEE Journal of Oceanic Engineering*, vol. 41, no. 3, pp. 509–514, 2016.

[7] W. Wang, T. Jost, and R. Raulefs, "Large scale characteristics of ship-to-land propagation at 5.2 GHz in harbor environment," in *Proceedings of the 2015 IEEE 82nd Vehicular Technology Conference (VTC2015-Fall)*, pp. 1–5, Boston, MA, USA, September, 2015.

[8] W. Wang, R. Raulefs, and T. Jost, "Fading characteristics of ship-to-land propagation channel at 5.2 ghz," in *Proceedings of the OCEANS 2016- Shanghai*, pp. 1–7, Shanghai, China, April, 2016.

[9] N. Mehrnia and M. K. Ozdemir, "Novel maritime channel models for millimeter radiowaves," in *Proceedings of the 2016 24th International Conference on Software, Telecommunications and Computer Networks (SoftCOM)*, pp. 1–6, Split, Croatia, September, 2016.

[10] K. Maliatsos, P. Loulis, M. Chronopoulos, P. Constantinou, P. Dallas, and M. Ikonomou, "Measurements and wideband channel characterization for over-the-sea propagation," in *Proceedings of the 2006 IEEE International Conference on Wireless and Mobile Computing, Networking and Communications*, pp. 237–244, Montreal, Canada, June, 2006.

[11] S. Jo, J. H. Jang, and W. Shim, "An analysis of path loss models of LTE-Maritime for mobile communication system in maritime environments," in *Proceedings of the 2019 22nd International Symposium on Wireless Personal Multimedia Communications (WPMC)*, pp. 1–5, Lisbon, Portugal, November, 2019.

[12] J.-H. Lee, J. Choi, W.-H. Lee, J.-W. Choi, and S.-C. Kim, "Measurement and analysis on land-to-ship offshore wireless channel in 2.4 GHz," *IEEE Wireless Communications Letters*, vol. 6, no. 2, pp. 222–225, 2017.

[13] C. Li, J. Yu, J. Xue, W. Chen, S. Wang, and K. Yang, "Maritime broadband communication: wireless Channel Measurement and characteristic analysis for offshore waters," *Journal of Marine Science and Engineering*, vol. 9, no. 7, p. 783, 2021.

[14] K. Yang, A. F. Molisch, T. Ekman, T. Roste, and M. Berbineau, "A round earth loss model and small-scale channel properties for open-sea radio propagation," *IEEE Transactions on Vehicular Technology*, vol. 68, no. 9, pp. 8449–8460, 2019.

[15] J. Wang, L. Guo, Y. Wei, and S. Chai, "Application of the improved SBR-TSM based on MPI to EM scattering from multiple targets above a 3-D rough sea surface," *IEEE Antennas and Wireless Propagation Letters*, vol. 21, no. 2, pp. 411–415, 2022.

[16] W. J. Pierson, *The Theory and Applications of Ocean Wave Measuring Systems at and below the Sea Surface, on the Land, from Aircraft, and from Spacecraft*, National Aeronautics and Space Administration, Washington, DC, USA, 1976.

[17] H. He, "A way to real-time ocean wave simulation," in *Proceedings of the International Conference on IEEE Computer Graphics, Imaging and Vision: New Trends, 2005*, Tianjin, China, August, 2005.

[18] A. Stogryn, "Equations for calculating the dielectric constant of saline water (correspondence)," *IEEE Transactions on Microwave Theory and Techniques*, vol. 19, no. 8, pp. 733–736, 1971.

[19] L. Klein and C. Swift, "An improved model for the dielectric constant of sea water at microwave frequencies," *IEEE Journal of Oceanic Engineering*, vol. 2, no. 1, pp. 104–111, 1977.

[20] W. L. Stutzman, *Polarization in Electromagnetic Systems*, Artech house, New York, NY, USA, 2018.

[21] A. R. Miller, R. M. Brown, and E. Vegh, "New derivation for the rough-surface reflection coefficient and for the distribution of sea-wave elevations," *IEE Proceedings H- Microwaves, Optics and Antennas*, vol. 131, no. 2, pp. 114–116, 1984.

[22] Z. Y. Liu and L. X. Guo, "A quasi three-dimensional ray tracing method based on the virtual source tree in urban microcellular environments," *Progress in Electromagnetics Research*, vol. 118, pp. 397–414, 2011.

[23] S. Jiang, W. Wang, Y. Miao, W. Fan, and A. F. Molisch, "A survey of dense multipath and its impact on wireless systems," *IEEE Open Journal of Antennas and Propagation*, vol. 3, pp. 435–460, 2022.